Check for updates

Two-step facile synthesis of Co_3O_4@C reinforced PbO_2 coated electrode to promote efficient oxygen evolution reaction for zinc electrowinning†

Wenhao Jiang,[ab] Junli Wang,[c] Xuanbing Wang, [iD] [ab] Jiang Liao,[a] Jinlong Wei,[b] Ruidong Xu [iD] *[ab] and Linjing Yang*[ab]

The conventional Pb–Ag alloy possesses a high oxygen evolution reaction overpotential, poor stability, and short service life in acidic solutions, making it an unsuitable sort of anode material for the zinc electrowinning process. Therefore, a layered carbon-covered cobalt tetroxide (Co_3O_4@C)-reinforced PbO_2-coated electrode is fabricated *via* a facile two-step pyrolysis-oxidation and subsequent electrodeposition process. As a result, the reinforced PbO_2-coated electrode exhibits a low OER overpotential of 517 mV at 500 A m^{-2} and a Tafel slope of 0.152 V per decade in a zinc electrowinning simulation solution (0.3 M $ZnSO_4$ and 1.53 M H_2SO_4). The reduced overpotential of 431 mV at 500 A m^{-2} compared to traditional Pb–0.76%Ag alloy leads to improved energy savings, which is attributable to the presence of Co_3O_4@C to refine the grain size and thus increase the effective contact area. Moreover, the reinforced PbO_2-coated electrode has a prolonged service life of 93 h at 20 000 A m^{-2} in 1.53 M H_2SO_4. Therefore, an accessible and efficient strategy for preparing a coated electrode to improve OER performance for zinc electrowinning is presented in this research.

1. Introduction

About 85% of zinc is currently extracted through hydrometallurgical electrowinning, but this process is economically burdensome due to high energy consumption.[1] In the zinc electrowinning process, the anode oxygen evolution reaction (OER) involves a four-electron transfer process resulting in slow kinetics, and its occurrence requires an ultrahigh overpotential, which is the dominant cause of the vast energy consumption.[2] Therefore, lowering the anodic OER overpotential is the principal direction for energy saving in the zinc electrowinning process.[3] Generally, Pb–(0.5–1%)Ag alloy is the most extensively employed insoluble anode.[4,5] However, its deficiencies, such as high overpotential, poor conductivity, and Pb contamination, are still tremendous challenges.[6,7]

Lead dioxide (PbO_2), as an inert metal oxide with the characteristics of good corrosion resistance and low price, is regularly prepared on the surface of Pb–(0.5–1%)Ag alloy in the zinc electrowinning industry.[8,9] Whereas further improvement is

urgently needed due to its inferior OER catalytic activity and poor stability in strongly acidic electrolytes.[10] Hence, the development of a PbO_2-coated electrode material with high electrocatalytic activity has always been the focus of research. For the past several decades, SnO_2–Sb_xO_y,[11,12] IrO_2–RuO_2,[13,14] and TiO_2 nanotubes (TiO_2-NTs)[15] have usually been fabricated as intermediate layers to improve the electrocatalytic activity and stability of PbO_2. In addition, some ions and active particles including Ag^{2+},[16,17] Ni^{2+},[18,19] Sn^{4+},[20] RuO_2,[21] CeO_2,[22] MnO_2,[23,24] carbon nanotubes (CNTs)[25] and Co_3O_4 (ref. 26 and 27) have been applied for reinforcing PbO_2 to achieve prominent OER electrocatalytic activity, thereby leading to lower energy consumption.

Cobalt-based oxide is a promisingly inexpensive and efficient OER catalyst.[28] Typically, it is reported that the unique spinel structure of Co_3O_4 facilitates electron transfer between cobalt ions in two different oxidation states: Co^{2+} occupying the tetrahedral sites and Co^{3+} located at the octahedral sites, offering more active sites and fewer energy barriers for the OER. And Co^{2+} is conducive to the formation of a CoOOH intermediate, which is the active site of the four-electron water splitting.[29] Nevertheless, it still has certain defects as a high-efficiency OER electrocatalyst. The surface energy of nanoscale Co_3O_4 increased as its size decreased, and it caused metal aggregation, dissolution and oxidation under long-term contact with the external environment, leading to a decrease in its electrocatalytic activity and stability. Moreover, Co_3O_4 was a p-type semiconductor with poor electrical conductivity, which

[a] State Key Laboratory of Complex Nonferrous Metal Resources Clean Utilization, Kunming University of Science and Technology, Kunming 650093, China. E-mail: eslinjingyang@kust.edu.cn; rdxupaper@aliyun.com

[b] Faculty of Metallurgical and Energy Engineering, Kunming University of Science and Technology, Kunming 650093, China

[c] Researcher Center for Analysis and Measurement, Kunming University of Science and Technology, Kunming 650093, China

† Electronic supplementary information (ESI) available. See DOI: 10.1039/d1ra09100j

hindered electron transfer and reduced the energy conversion efficiency.[26,30] As a substance with stable properties, carbon is an ideal material for improving the stability of transition metal-based catalysts.[31] Therefore, it has been found that using carbon materials to coat metal nanoparticles is an effective improvement strategy to avoid the contact of internal metals with the external environment and improve the stability of the catalyst.[32]

Accordingly, we synthesized a Co_3O_4@C-reinforced PbO_2-coated electrode by a simple two-step pyrolysis-oxidation and subsequent electrodeposition process. The morphology and structure were characterized by scanning electron microscopy (SEM), transmission electron microscopy (TEM), X-ray diffraction (XRD), and X-ray photoelectron spectroscopy (XPS), while other electrochemical tests were used to measure the electrochemical performance. Notably, a Co_3O_4@C-reinforced PbO_2-coated electrode showed excellent OER activity and long service life in zinc electrowinning simulation solution (0.3 M $ZnSO_4$ and 1.53 M H_2SO_4). In comparison with a conventional Pb–0.76%Ag electrode, the reinforced PbO_2 electrode possessed a reduced η value of 431 mV at 500 A m^{-2}, which significantly reduced the energy consumption. In addition, it exhibited strong durability with a service life of up to 93 h in 1.53 M H_2SO_4 at 20 000 A m^{-2}.

2. Experimental

2.1 Materials

Polyvinyl pyrrolidone (PVP) ($M_w \approx 1\ 300\ 000$), cobalt nitrate hexahydrate ($Co(NO_3)_2 \cdot 6H_2O$), lead nitrate ($Pb(NO_3)_2$), lead oxide yellow (PbO), nitric acid (HNO_3), and sodium hydroxide (NaOH) were procured from Aladdin. Pb–0.6%Sb plates were provided by the Kunming Hendera company. All chemicals were analytically pure and ready for use without further purification.

2.2 Synthesis of the Co_3O_4@C composite

In a typical synthesis of Co_3O_4@C composite, $Co(NO_3)_2 \cdot 6H_2O$ (1.7 g) and PVP powder (2 g) were dissolved in 15 mL of DI water, then stirred intensively for 1 h and dried in a drying oven at 70 °C for 15 h. Then the Co_3O_4@C composite was prepared by pyrolysing at 750 °C for 2 h under an N_2 atmosphere followed by oxidation in air at 250 °C.

2.3 Preparation of PbO_2-coated electrode

To begin with, a Pb–0.6%Sb/α-PbO_2 electrode was prepared by electrodeposition in an alkaline system (0.15 M PbO and 3 M NaOH) at 15 mA cm^{-1}. Then, the Co_3O_4@C-reinforced PbO_2-coated electrode was prepared by constant-current electrodeposition in a solution consisting of 0.8 M $Pb(NO_3)_2$, 0.03 M HNO_3, and a specific amount of Co_3O_4@C. A previously prepared Pb–0.6%Sb/α-PbO_2 electrode was applied as the anode and a stainless steel sheet was employed as the cathode. The electrodeposition process proceeded at 25 mA cm^{-2} in a 40 °C thermostatic water bath for 1 h. After the reaction, the sample was taken out and dried at room temperature for subsequent testing.

2.4 Characterization

The crystalline structures of the Co_3O_4@C composite and PbO_2-coated electrodes were characterized using X-ray diffraction (XRD) measurement and X-ray photoelectron spectroscopy (XPS, PHI5500). The morphology and microstructure of the Co_3O_4@C composite were identified with field-emission scanning electron microscopic (FE-SEM; Nova NanoSEM 450) and transmission electron microscopic (TEM) measurements. Raman spectra were documented utilizing a LabRAM HR evolution Raman spectrometer. Fourier-transform infrared (FT-IR) spectra were performed using a Bruker ALPHA (Germany) spectrometer.

2.5 Electrochemistry

All electrochemical tests were performed utilizing an electrochemical workstation equipped with a traditional three-electrode cell in zinc electrowinning simulation solution (0.3 M $ZnSO_4$ and 1.53 M H_2SO_4) at 35 °C. All electrochemical tests in this work were performed without iR compensation. The PbO_2-coated electrode served as a working electrode with an effective area of 1 cm^2. A saturated calomel electrode (SCE) and stainless-steel dish were used for the reference and counter electrodes, respectively.

3. Results and discussion

3.1 Fabrication and characterization

The graphical representation in Fig. 1a shows that the Co_3O_4@C composite was synthesized by pyrolysis in a tube furnace, followed by oxidation. PVP and $Co(NO_3)_2 \cdot 6H_2O$ served as the carbon and cobalt sources, respectively. After the pyrolysis-oxidation process, the prepared Co_3O_4@C composite served as an electrochemically active modifier for subsequent electrodeposition. The PbO_2 electrodeposition mechanism in Fig. 1b can be described according to previously studied literature.[33,34] A Co_3O_4@C-reinforced PbO_2-coated electrode with a layered structure was fabricated via electrodeposition. As depicted in Fig. 1c, the layered Co_3O_4@C-reinforced PbO_2-coated electrode consisted of three layers, with Pb–0.6%Sb alloy as the substrate, α-PbO_2 as the intermediate layer to strengthen the combination of the substrate and the β-PbO_2 layer, and the outermost β-PbO_2-Co_3O_4@C as the active layer for boosting OER activity.

The X-ray diffraction (XRD) pattern of Co_3O_4@C is recorded in Fig. 2a. The outstanding diffraction peaks at 19.0, 31.2, 36.8, 38.5, 44.8, 55.7, 59.4, and 65.2° can be well indexed to the (111), (220), (311), (222), (400), (422), (511) and (440) lattice planes of pure spinel Co_3O_4 without any evident impurities. The Raman spectrum (Fig. 2b) was collected in the range of 100–2000 cm^{-1} and showed five evident vibrational bands at 205, 482, 527, 618, and 691 cm^{-1}, indexed to F_{2g} 205, E_g 482, F_{2g} 527, F_{2g} 618, and A_{1g} 691 symmetry modes, respectively. All five identified peaks accurately matched the pure Co_3O_4 spinel structure. Moreover, in Fig. 2b, the D band (due to the highly ordered graphite lattice)[35] can be observed at 1349.35 cm^{-1} and the G band (given the sp^2 carbon)[36] at 1593.39 cm^{-1}. These two bands were in accord with the characteristic D and G vibrational bands of
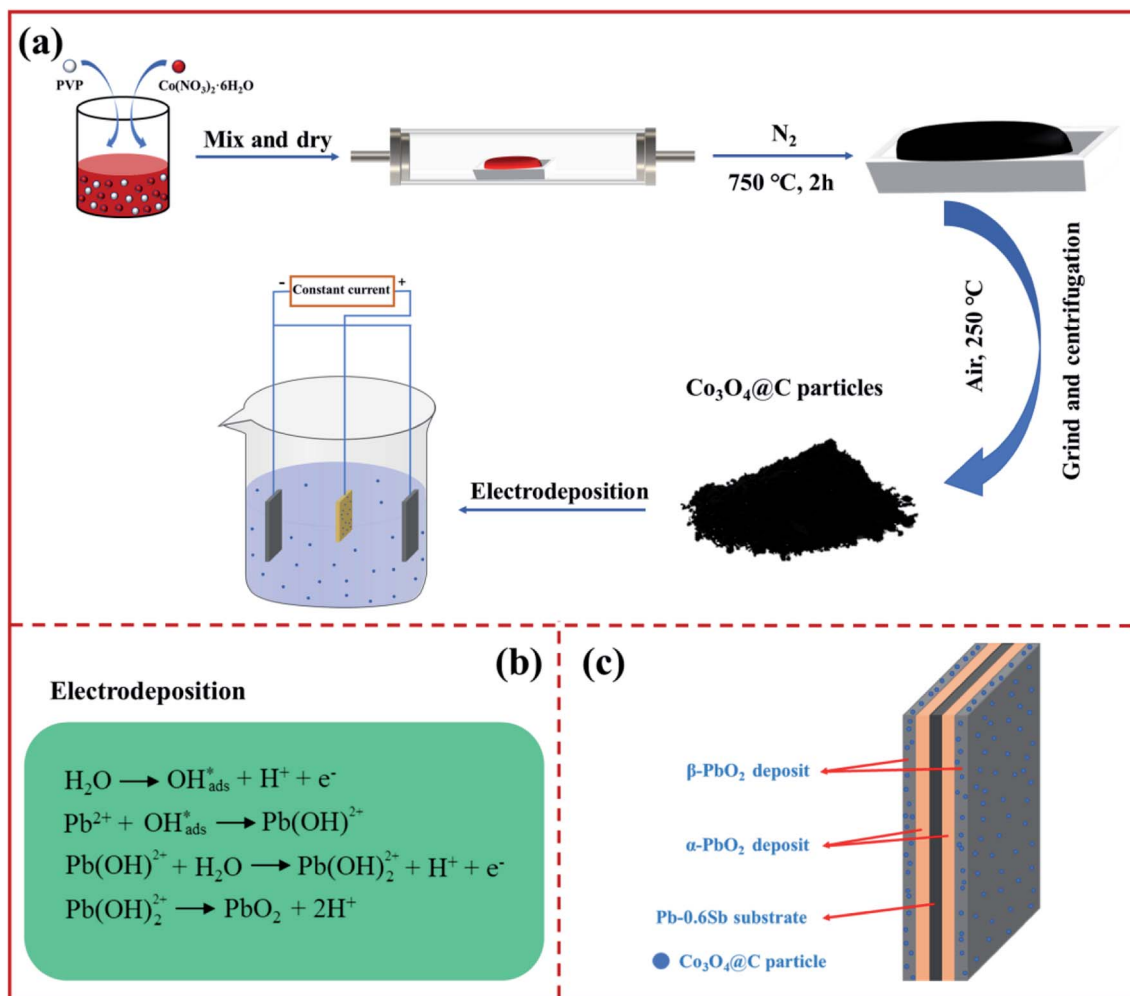
Fig. 1 An illustration of (a) the fabrication procedure, (b) equations of the lead dioxide deposition mechanism, and (c) the construction of a layered Co_3O_4@C-reinforced PbO_2-coated electrode.

graphitic carbon that may be produced by PVP carbonization. The composition of the Co_3O_4@C composite was further verified by the FT-IR spectrum (Fig. 2c). In terms of details, the absorption band at 1403.42 cm^{-1} was assigned to the O–H stretching vibration in absorbed water, while the O–H deformation vibration band in absorbed water was observed at 3416.94 cm^{-1}.[37] The band at 1636.42 cm^{-1} derived from C=O groups. The Co–O bond characteristic of the Co_3O_4@C composite was investigated in the intensive bands at 662.97 and 564.61 cm^{-1}.[38]

XPS measurements were carried out to characterize the chemical states and structure of the Co_3O_4@C composite. Fig. S1† exhibits the overall XPS spectra to confirm the main Co, O, C elements with their characteristic peaks for Co 2p, O 1s, and C 1s at 780.0, 529.6, and 284.8 eV binding energies, respectively. Two prominent peaks in Fig. 2d located at 779.74 and 795.34 eV were related to Co $2p_{3/2}$ and Co $2p_{1/2}$, respectively, indicating spin–orbit doublets and the formation of Co_3O_4. In addition, two related satellite peaks were fitted at 775.59 and 803.84 eV, further denoting the coexistence of Co^{2+} and Co^{3+} oxidation states. The Co $2p_{3/2}$ and the Co $2p_{1/2}$ peaks can be

further separated into two peaks. The peaks located at 780.65 and 796.03 eV were identified as Co^{2+}. And the other two peaks positioned at 779.28 and 794.88 eV were correlated with Co^{3+} in the Co_3O_4@C composite.[39]

As displayed in Fig. 2e, in the high-resolution XPS spectra of O 1s, there were three deconvoluted peaks representing chemisorbed oxygen (O_c) at 528.77 eV, lattice oxygen (O_L) at 529.86 eV, and oxygen vacancies (O_v) at 531.98 eV.[31,40] The high-resolution C 1s spectrum (Fig. 2f) revealed the existence of four species, which were associated with C=C (283.53 eV), C–C (284.14 eV), C–O (284.92 eV), and C=O (286.18 eV).[41,42] Notably, oxygen-containing groups (C–O and C=O) were beneficial for enhancing the hydrophilicity of Co_3O_4@C, leading to facilitating the absorption of H_2O molecules on the catalyst surface, thus improving the OER activity in an acidic electrolyte.[40,43]

The morphology and microstructure examined *via* SEM and TEM images of the prepared Co_3O_4@C composite are summarized in Fig. 3. In the SEM image (Fig. 3a), numerous spherical nanoparticles in a diameter range from 55 to 85 nm overlapped to form large-sized clusters, which is consistent with the morphology revealed by the dark spots of the low-magnification
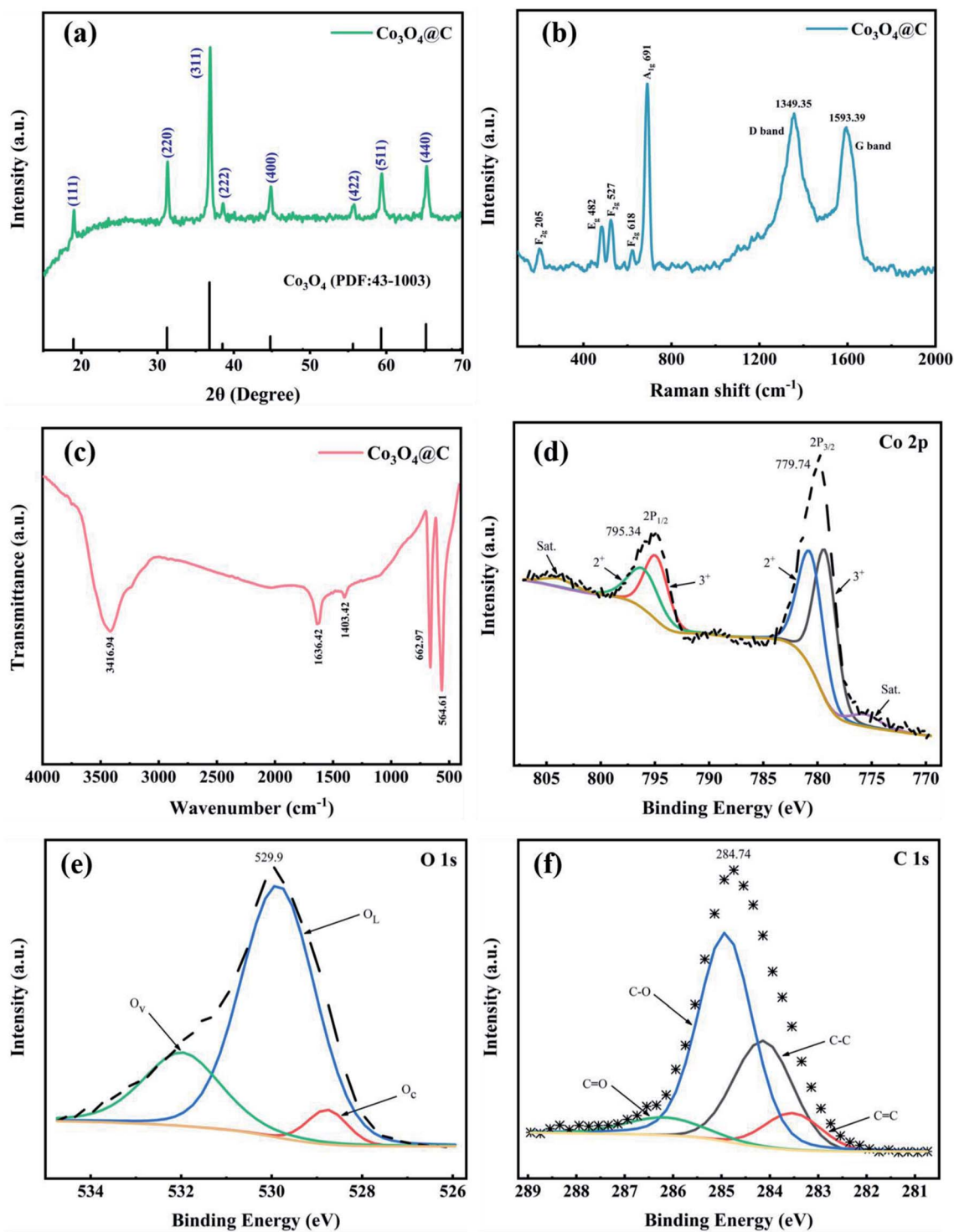
Fig. 2 (a) XRD pattern, (b) Raman and (c) FT-IR spectra, high-resolution XPS spectra for (d) Co 2p, (e) O 1s and (f) C 1s of the as-prepared Co$_3$O$_4$@C composite.

TEM images. From the elemental mappings (Fig. 3b), the Co, O, and C elements were uniformly distributed and were the main components of Co$_3$O$_4$@C, which further proved the coexistence of Co, O, and C in the prepared Co$_3$O$_4$@C composite. A detailed examination of the HRTEM (Fig. 3e) showed that the lattice fringes were arrayed in a legible and disciplined manner. The

interplanar spacing of 0.47 nm, corresponding to the (111) plane of spinel Co$_3$O$_4$, was clearly observed. Besides, it can be seen that crystalline Co$_3$O$_4$ was covered with amorphous carbon involving inconspicuous lattice fringes across the obvious interface, which was in keeping with the spherical structure of the nanoparticles exhibiting a layer of carbon wrapped around
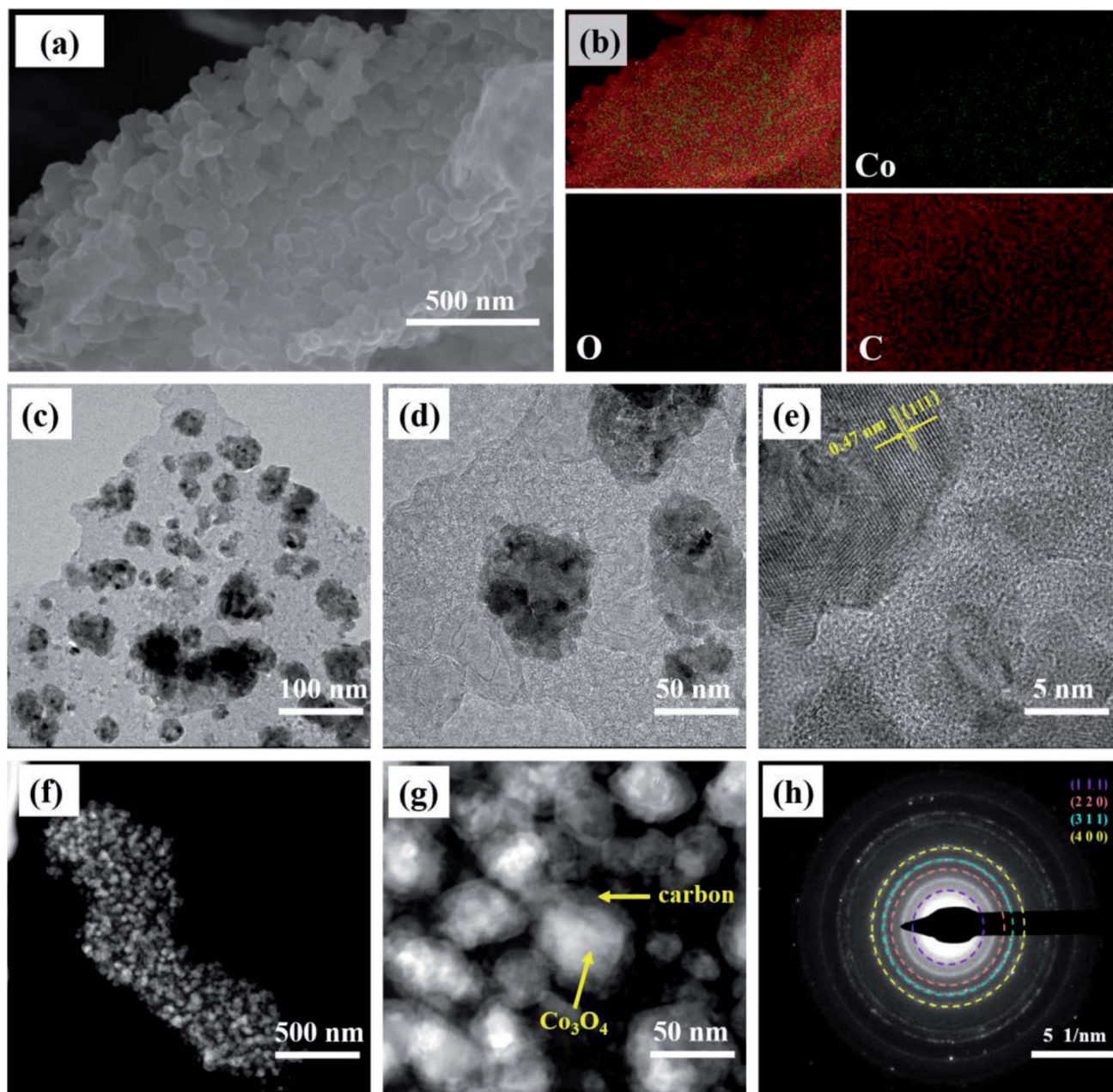
Fig. 3 (a) The SEM image, (b) elemental mapping, (c and d) and (f and g) TEM images, (e) HRTEM image, and (h) SAED pattern of the Co_3O_4@C composite.

them in Fig. 3f and g. Fig. 3h exhibits a selected area electron diffraction (SAED) pattern, suggesting that the Co_3O_4 composite was well crystallized with a polycrystalline essence. The several diffraction rings corresponded to the (111), (220), (311), and (400) planes of the Co_3O_4 composite. As detailed above for all characterizations, the elemental composition and phase information of the spinel Co_3O_4 and carbon were precisely determined utilizing the XRD, Raman, FT-IR, and XPS spectra. And the morphology and nanostructure of the Co_3O_4 composite were subsequently investigated using SEM and TEM images, which revealed the co-existence of crystalline Co_3O_4 and amorphous carbon in an encapsulated state.

The XRD patterns of PbO_2 deposited without and with reinforcement by Co_3O_4@C are recorded in Fig. 4a. Specifically, according to the standard data (JCPDS, no. 41-1492), the significant peaks located at 25.43°, 31.97°, 36.19°, 49.04°, 62.46°, and 74.41° were assigned to (110), (101), (200), (211), (301) and (321) planes, respectively, which were associated with β-PbO_2. The related characteristic peaks of α-PbO_2 were found at 28.62°, 36.16°, 49.49°, matching well with the (111), (200) and (130) crystal planes (JCPDS, no. 45-1416). The existence of Co_3O_4@C was not detected from this XRD measurement, which may be caused by the low content of Co_3O_4@C in the deposit. Furthermore, it was found that the addition of Co_3O_4@C
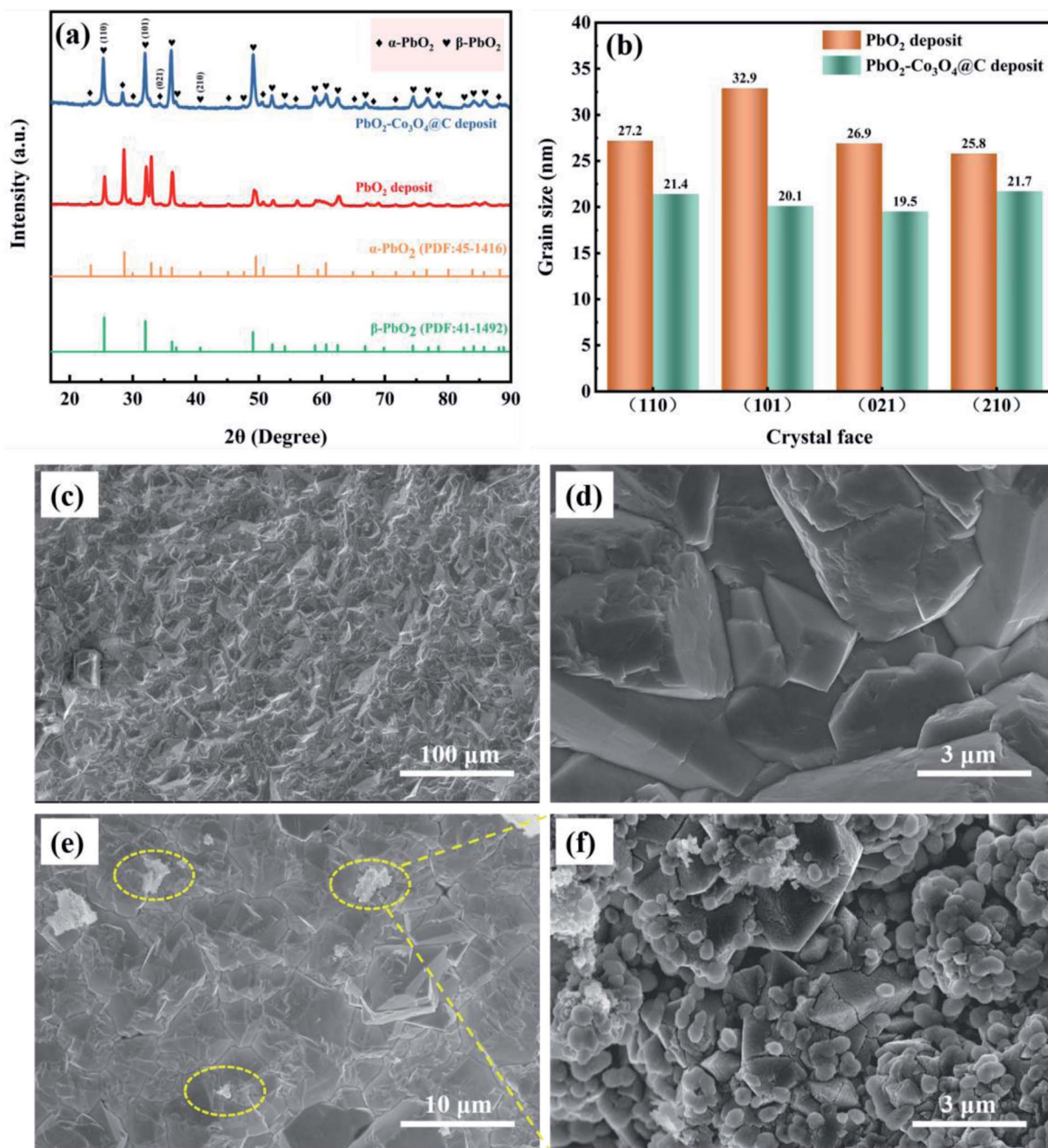
Fig. 4 (a) The XRD patterns, (b) a comparison of grain size of different crystal planes, and the SEM images of (c and d) β-PbO$_2$ and (e and f) β-PbO$_2$-Co$_3$O$_4$@C sedimentary layers.

weakened the intensity of the diffraction peak, which was beneficial for reducing the crystal grain size since the half-width height of the diffraction peak was negatively correlated with the grain size according to Debye–Scherrer's eqn (1). It is also worth noting that the characteristic diffraction peaks of Co$_3$O$_4$ and carbon were not observed in the XRD measurement, which may be explained by the small amount in the electrode. Hence, the grain sizes of the (110), (101), (021), and (210) crystal planes were calculated with eqn (1), and the calculations are plotted in Fig. 4b.

$$D = \frac{K\lambda}{\beta \cos \theta} \qquad (1)$$

where D refers to the average thickness perpendicular to the direction of the crystal plane, K is the K-Scherrer constant (0.89), λ indicates the X-ray wavelength (0.15405 nm), β represents the half-width height of the diffraction peak, and θ stands for the diffraction angle.[44–46] As exhibited in Fig. 4b, the grain size of PbO$_2$–Co$_3$O$_4$@C was somewhat reduced compared to the PbO$_2$ deposit, which gave rise to an increase in electrochemical surface area. To gain more insight into changes in the

electrochemically active area (ECSA), we measured capacitive current versus scan rate for the PbO_2 and PbO_2–Co_3O_4@C deposits in Fig. S2.† The C_{dl} values of the PbO_2 and PbO_2–Co_3O_4@C deposits (Fig. S2c†) were measured to be 13.6 and 26.5 mF cm^{-2}, respectively. This comparison showed that the presence of Co_3O_4@C was indeed beneficial to increasing the ECSA of PbO_2. Therefore, it can barely be determined whether Co_3O_4@C was co-deposited into the β-PbO_2 deposit by XRD alone.

To clarify the role of α-PbO_2, Fig. S3† shows cross-sectional SEM images of Pb–0.6%Sb/β-PbO_2 and Pb–0.6%Sb/α-PbO_2/β-PbO_2 electrodes. As can be seen in Fig. S3a,† the thickness of the α-PbO_2 layer was around 50 μm while the thickness of the β-PbO_2 layer was in range of 105 to 165 μm. There were no obvious structural defects at the interface among the substrates, α-PbO_2 and β-PbO_2, and the structure was dense and uniform. However, in Fig. S3b,† the interface between the substrate and β-PbO_2 is more obviously heterogeneous, which caused the PbO_2 electrode to have poor durability in harsh environments. Therefore, in this work, a layer of α-PbO_2 was electrodeposited to improve the bonding between the substrate and the β-PbO_2 active layer, thus improving the lifetime of the whole PbO_2 electrode. Fig. 4c and d show the images of β-PbO_2 without reinforcement by Co_3O_4@C at high and low magnification. It can be found that β-PbO_2 exhibited a regular pyramidal morphology which can effectively increase the contact area and thus lead to a speedy OER. Fig. 4e shows a β-PbO_2-Co_3O_4@C deposit at low magnification, and Fig. 4f shows a partial high-magnification view. The Co_3O_4@C composite can be seen in the β-PbO_2 deposit, confirming that Co_3O_4@C and PbO_2 co-deposited to form the Co_3O_4@C-reinforced PbO_2-coated electrode. To highlight this, Fig. S4† shows the SEM image and element map of the PbO_2–Co_3O_4@C deposit. From the SEM image, it could be found that numerous Co_3O_4@C particles overlaid a portion of the pyramidal β-PbO_2. The elemental map exhibited a uniform distribution of the four elements Pb, Co, O, and C, which further demonstrated the coexistence of PbO_2 and Co_3O_4@C.

3.2 Electrochemical performance

Fig. S5† displays the linear sweep voltammetry (LSV) curves of electrodes without reinforcement and reinforced by the prepared Co_3O_4@C composite with different oxidation times (OTs). To explore the best oxidation time, the Co_3O_4@C composite was fabricated through oxidation in air at 250 °C for 1 hour, 3 hours, 5 hours, and 7 hours, respectively. One can see that the Pb–0.6%Sb/α-PbO_2/β-PbO_2-Co_3O_4@C (OT = 3 h) electrode exhibited the lowest potential of 1.516 V at 500 A m^{-2}, which was remarkably reduced by 431 mV compared with the unreinforced electrode (Pb–0.6%Sb/α-PbO_2/β-PbO_2). The potentials of other reinforced PbO_2 electrodes were 1.680 V (Pb–0.6%Sb/α-PbO_2/β-PbO_2-Co_3O_4@C, OT = 1 h), 1.517 V (OT = 5 h), and 1.569 V (OT = 7 h), respectively. Fig. S6† shows the OER overpotential of all the electrodes mentioned above at 500 A m^{-2}. As depicted, the Pb–0.6%Sb/α-PbO_2/β-PbO_2-Co_3O_4@C (OT = 3 h) electrode exhibited the lowest overpotential of 517 mV.

Obviously, Co_3O_4@C (OT = 3 h) showed the most excellent catalytic activity. Therefore, over the whole context, the Co_3O_4@C (OT = 3 h) composite and Pb–0.6%Sb/α-PbO_2/β-PbO_2-Co_3O_4@C (OT = 3 h) with different concentrations will be discussed.

The cyclic voltammetry (CV) curves of the Co_3O_4@C-reinforced PbO_2-coated electrodes with different concentrations are shown in Fig. 5a. All electrodes possessed a strong oxidation peak, indicating the splitting of H_2O into O_2. And all the reduction peaks can be correlated with the formation of Pb^{2+} ($PbSO_4$), as given in the formula below:

$$PbO_2 + H_2SO_4 + 2H^+ + 2e^- \leftrightarrow PbSO_4 + 2H_2O \qquad (2)$$
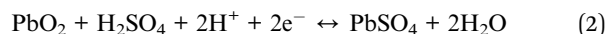
The redox performance of all PbO_2 electrodes seemed to be similar. It is worth noting that the reduction peak in the cathodic branch of the Pb–0.6%Sb/α-PbO_2/β-PbO_2-Co_3O_4@C (0 g L^{-1}) electrode showed a significantly negative shift, which may be due to the susceptibility of the unreinforced electrode to changes in solution composition during the test.[47]

Fig. 5b displays the LSV curves of all PbO_2-coated electrodes with different Co_3O_4@C concentrations. The order of oxygen evolution potential at 500 A m^{-2} from high to low is Pb–0.6%Sb/α-PbO_2/β-PbO_2 (0 g L^{-1}) (1.947 V) > Pb–0.6%Sb/α-PbO_2/β-PbO_2-Co_3O_4@C (8 g L^{-1}) (1.670 V) > Pb–0.6%Sb/α-PbO_2/β-PbO_2-Co_3O_4@C (10 g L^{-1}) (1.655 V) > Pb–0.6%Sb/α-PbO_2/β-PbO_2-Co_3O_4@C (2 g L^{-1}) (1.619 V) > Pb–0.6%Sb/α-PbO_2/β-PbO_2-Co_3O_4@C (6 g L^{-1}) (1.575 V) > Pb–0.6%Sb/α-PbO_2/β-PbO_2-Co_3O_4@C (4 g L^{-1}) (1.516 V). As represented in Fig. S7,† the corresponding order of overpotential is 948, 671, 656, 620, 576, and 517 mV, respectively. Evidently, when the electrodeposition concentration of Co_3O_4@C was 4 g L^{-1}, the reinforced PbO_2 electrode exhibited the lowest overpotential, suggesting the most excellent OER electrocatalytic activity. Hence, the concentration of Co_3O_4@C in the electrolyte of 4 g L^{-1} was considered the best condition for preparing composite electrodes. Furthermore, Fig. S8† shows the relationship among the Co_3O_4@C concentration, the loading mass, and the percentage of Co_3O_4@C mass in the active β-PbO_2 layer. When the concentration of Co_3O_4@C was raised from 0 to 4 g L^{-1}, the loading mass showed a significant increase. However, the increasing trend of the loading mass was more gradual when the concentration exceeded 4 g L^{-1}. This regularity also confirmed that the Co_3O_4@C-reinforced PbO_2-coated electrode (4 g L^{-1}) had minimum OER overpotential in Fig. S7.† Therefore, 4 g L^{-1} Co_3O_4@C in the electrolytic solution was considered the best concentration conditions to prepare the coated electrodes.

From Fig. 5c, one can see that the LSV curves were processed with the Tafel equation ($\eta = a + b \lg i$) to obtain the Tafel linear fitting lines for all PbO_2 electrodes. Related factors are listed in Table S1.† All R^2 values exceeded 0.99, indicating the accuracy of the fitting. It can be observed from Table S1† (column b) that all Co_3O_4@C-reinforced PbO_2-coated electrodes showed lower OER values, indicating that their OER kinetics were enhanced. In particular, the Co_3O_4@C-reinforced PbO_2-coated electrode (4 g
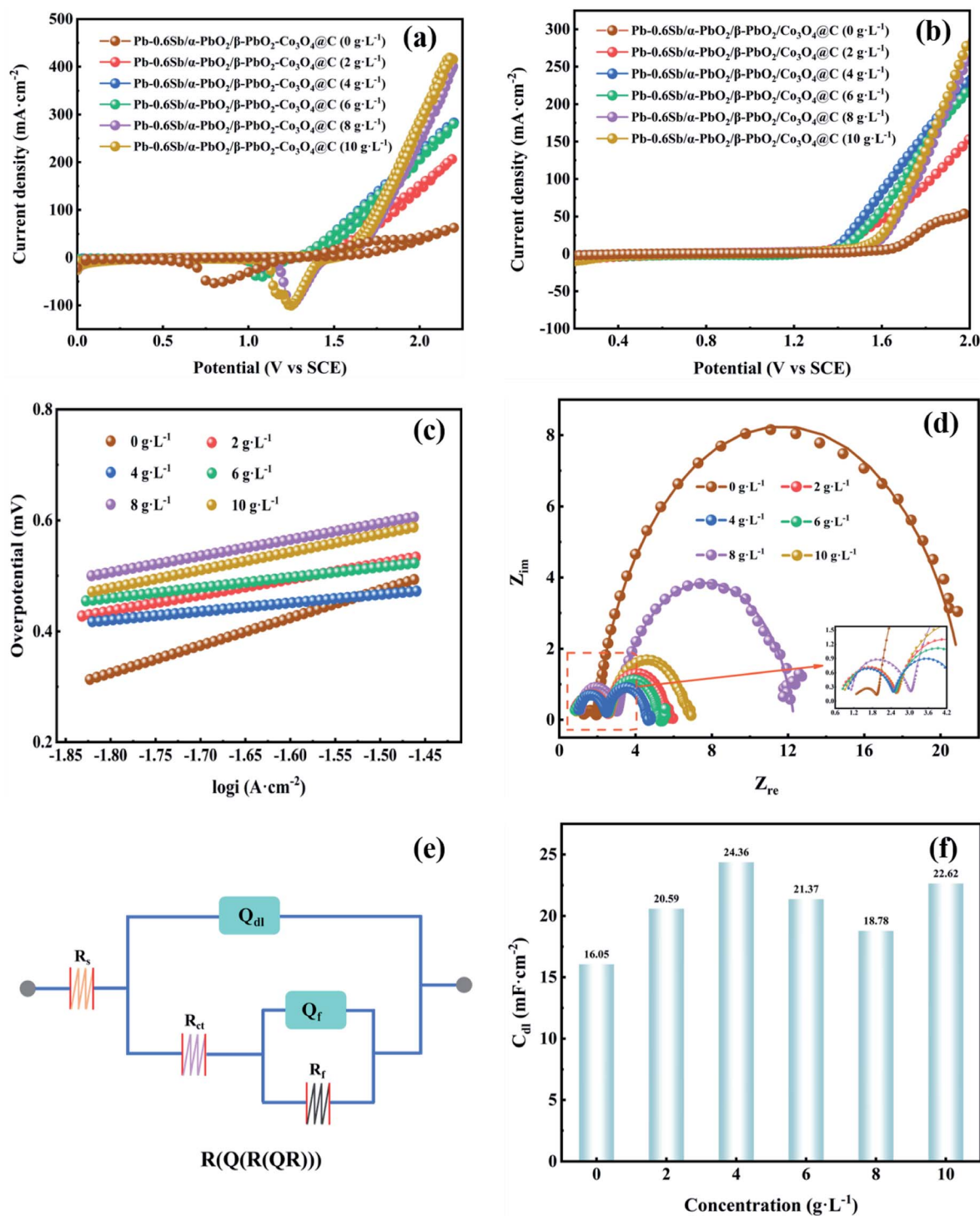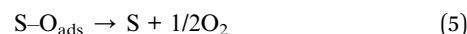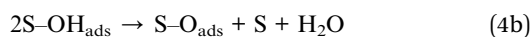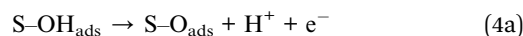
Paper

Fig. 5 (a) CV curves, (b) LSV curves, (c) related Tafel fitting plots, (d) electrochemical impedance spectroscopy Nyquist plots, (e) equivalent circuit, (f) C_{dl} values of the PbO_2-coated electrode reinforced with different concentrations of $Co_3O_4@C$.

L^{-1}) showed a minimum Tafel slope value of 0.156 V dec^{-1}, which denoted the fastest oxygen evolution reaction kinetics.

A widely recognized OER pathway could be elaborated in detail using formulae (3)–(5):[48,49]

$$S + H_2O \rightarrow S\text{–}OH_{ads} + H^+ + e^- \tag{3}$$

$$S\text{–}OH_{ads} \rightarrow S\text{–}O_{ads} + H^+ + e^- \tag{4a}$$

$$2S\text{–}OH_{ads} \rightarrow S\text{–}O_{ads} + S + H_2O \tag{4b}$$

$$S\text{–}O_{ads} \rightarrow S + 1/2O_2 \tag{5}$$

where S represents the real active sites on the coated electrode surface, while S–OH$_{ads}$ and S–O$_{ads}$ denote the adsorbable hydroxyl- and oxygen-group species, respectively. What is noticeable is that the rate-determining step (rds) for a specific electrode is usually related to the Tafel slope of OER. As shown from previous studies, when the Tafel slope is similar to or larger than 0.12 V dec^{-1}, formula (3) – the formation and adsorption of first intermediate S–OH$_{ads}$ – can be regarded as the rds.[48] All b values in Table S1† are larger than 0.12 V dec^{-1}, indicating that reaction (3) is the rds.

To improve our understanding of the electrochemical performance of all PbO$_2$ electrodes, EIS measurements were employed to examine the charge transfer property of the electrode–solution interface in the frequency region of 0.01–100 000 Hz. As displayed in Fig. 5d, the Nyquist plots of all PbO$_2$ electrodes showed a similar shape consisting of two semicircles located in the high-frequency and low-frequency regions, respectively. The high-frequency semicircle represents the adsorption resistance (R_f) of the OER intermediates (S–OH$_{ads}$ and S–O$_{ads}$), and the low-frequency semicircle represents the charge transfer resistance (R_{ct}).[15,50] Each electrode exhibited a low adsorption resistance (R_f) value, reaching the smallest one when Co$_3$O$_4$@C electrodeposition concentration was 4 g L^{-1}. And the radius of curvature of the low-frequency semicircle in the Nyquist plot was smallest when the Co$_3$O$_4$@C electrodeposition concentration was 4 g L^{-1}, implying the smallest charge transfer resistance (R_{ct}) (2.18 Ω). The equivalent circuit of $R(Q(R(QR)))$ (Fig. 5e) was utilized to model the electrochemical system, where the R_s was the solution resistance, Q_{dl} was a constant phase element associated with the bilayer capacitance (C_{dl}) on the (Pb–0.6%Sb substrate|coated layers|electrolytic solution) and Q_f was another constant-phase element, and R_f was the adsorption resistance. All the calculations are listed in Table S2.† The R_s values of all PbO$_2$ electrodes fluctuated over a small range, indicating that the tested solutions were in a similar steady-state. For Q_{dl}, the bilayer capacitance C_{dl} was derived from formula (6), and all calculations are plotted in Fig. 5f. Obviously, the reinforced PbO$_2$ electrode with the Co$_3$O$_4$@C concentration of 4 g L^{-1} possessed the largest C_{dl} value. Among all PbO$_2$ electrodes, the Co$_3$O$_4$@C-reinforced PbO$_2$-coated electrode (4 g L^{-1}) showed minimum R_f (0.12 Ω), R_{ct} (2.18 Ω) and maximum C_{dl} (24.36 mF cm^{-2}) values, demonstrating the most significant OER electrocatalytic activity.[51]

$$C = Q^{1/n} R_s^{(1-n)/n} \qquad (6)$$

Fig. S9† is a histogram comparing the overpotential at 500 A m^{-2} of various electrodes investigated in the literature and this study, and the relevant references cited are listed in Table S3.† Notably, the overpotential of the Co$_3$O$_4$@C-reinforced PbO$_2$-coated electrode (4 g L^{-1}) in this work was the lowest compared with other electrodes. The possible reasons are as follows: (1) the presence of Co$_3$O$_4$@C composite refined the crystal grains, thereby increasing its contact surface area; (2) the existence of carbon not only increased the electrical conductivity but prevented the internal metal oxide from contacting the outside,

consequently providing a stable electrochemical reaction interface; (3) the intrinsic OER electrocatalytic performance of the Co^{2+}/Co^{3+} redox couple generated more active sites to promote the OER and (4) the Co$_3$O$_4$@C composite significantly expanded the active surface area, reduced the R_{ct} value and promoted rapid electron transfer. The combined effects of these four aspects promoted enhanced OER electrocatalytic activity.

The potential of Co$_3$O$_4$@C in the suspension was measured with a zeta potential analyzer (90Plus Zeta, Brookhaven Instruments Corporation), and the sedimentation time of Co$_3$O$_4$@C in the suspension was recorded with photographs to figure out the nature of the Co$_3$O$_4$@C suspension. The zeta potential values of Co$_3$O$_4$@C measured in Fig. S10† were all negative, indicating that the Co$_3$O$_4$@C particles were negatively charged in this plating system and the electric field force caused Co$_3$O$_4$@C to co-deposit with PbO$_2$ at the anode. In Fig. S11,† when the time reached 90 min, the vast majority of Co$_3$O$_4$@C particles had settled at the bottom of the bottle. Whereas the suspension was constantly being stirred during the electrodeposition process, so the original dispersion state of the suspension could always be maintained. As is vividly depicted in Fig. S12,† the negatively charged Co$_3$O$_4$@C particles migrated to the anode because of stirring and the electric field forces and were then embedded in the β-PbO$_2$ deposit.

3.3 The zinc electrowinning simulation experiment

In order to evaluate the OER stability, service life tests of the three electrodes were performed at a current density of 500 A m^{-2} for 50 000 s in a zinc electrodeposition simulation solution (0.3 M ZnSO$_4$ and 1.53 M H$_2$SO$_4$) and the corresponding galvanostatic polarization curves are recorded in Fig. 6a. When the electrowinning reached a steady-state, the order of the average potential from large to small is 1.925, 1.907, 1.516 V, in accordance with the Pb–0.76%Ag alloy, Pb–0.6%Sb/α-PbO$_2$/β-PbO$_2$, and Pb–0.6%Sb/α-PbO$_2$/β-PbO$_2$-Co$_3$O$_4$@C electrodes, respectively. Apparently, the Co$_3$O$_4$@C-reinforced PbO$_2$-coated electrode (4 g L^{-1}) had strong stability and the lowest steady-state potential, leading to enhanced OER activity. However, the stability of the PbO$_2$ electrode prepared in this work still needed to improve. The improvement methods that have been reported in the literature to enhance the stability of the electrode could be learned from. For instance, TiO$_2$ nanotubes/network as an interlayer and gas electrodes made of carbon black (CB) supported on a titanium grid and combined with polytetrafluoroethylene (PTFE) have shown good stability in the field of electrochemistry.[52–54]

The cell voltage of the zinc electrowinning process was the leading cause of excessive energy consumption, which consisted of the following five main components:

$$U_c = IR_1 + IR_2 + IR_3 + IR_4 + IR_5 \qquad (7)$$

where U_c referred to the cell voltage, IR_1 stood for the voltage drop of zinc sulfate decomposition, IR_2 denoted the electrolytic solution resistance voltage drop, IR_3 indicated the voltage drop of bipolar resistance, IR_4 represented the contact resistance
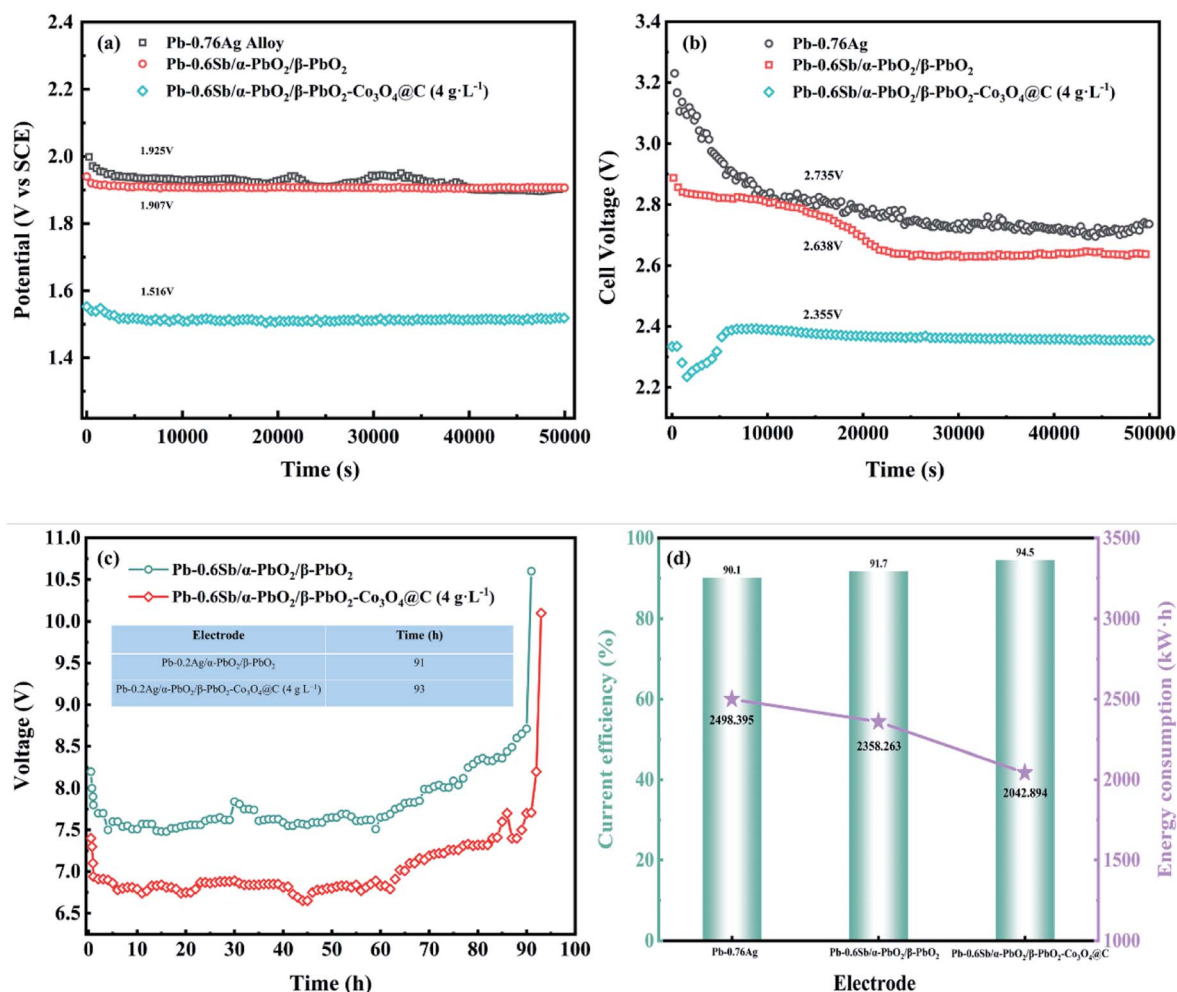
Fig. 6 (a) Galvanostatic polarization curves, (b) cell voltage, (c) service life, and (d) current efficiency and tonne of zinc electricity consumption of different electrodes in the zinc electrowinning simulation experiment.

voltage drop, and IR_5 was the resistance voltage drop of anode slime.

The cell voltages of the three electrodes over 50 000 s are illustrated in Fig. 6b. In the early stage of electrowinning, the Co_3O_4@C-reinforced PbO_2-coated electrode gradually stabilized after 5000 s; however, the other two electrodes tended to stabilize after 20 000 s, which showed the remarkable stability of the Co_3O_4@C reinforced PbO_2-coated electrode and was consistent with the results of galvanostatic polarization measurement. As plotted in Fig. 6b, the cell voltage of the Co_3O_4@C-reinforced PbO_2-coated electrode (4 g L^{-1}) is a minimum of 2.355 V, which is 380 mV lower than the Pb–0.76%Ag alloy, showing an outstanding energy-saving effect. Furthermore, the lower cell voltage value for Pb–0.76%Ag compared to industrial applications was mainly because the laboratory's zinc electrowinning simulation solution was configured using deionized water, which had few impurity ions in the solution.

Fig. 6c displays the service life of the electrode with and without reinforcement at an ultra-high current density of 20 000 A m^{-2}. As shown in this figure, the Co_3O_4@C-reinforced PbO_2-

coated electrode (4 g L^{-1}) can serve 93 hours in a strongly acidic electrolyte (1.53 M H_2SO_4), demonstrating excellent corrosion resistance. As two essential economic indicators in the zinc electrowinning simulation experiment, the calculated current efficiency and tonne of zinc electricity consumption values are drawn in Fig. 6d. The current efficiency (η) is the proportion of actual Zn deposition to theoretical Zn deposition and was calculated according to eqn (8) (m represents the actual amount of Zn deposited during time t (g), I is the current (A), t refers to the deposition time (h), n stands for the quantity of electrolytic tanks, and q denotes the electrochemical equivalent of Zn (1.22 g A^{-1} h^{-1})). Calculations suggested that the Co_3O_4@C-reinforced PbO_2-coated electrode had the highest current efficiency of 94.5%. The slightly lower current efficiency of the Pb–0.76%Ag alloy may be due to the gradual oxidation of the surface to produce PbO_2 oxide film, which consumed some of the current. The tonne of zinc electricity consumption (W) of the three composite electrodes was calculated from eqn (9) (v represents the cell voltage, η represents the current efficiency). The tonne of zinc electricity consumption of the Co_3O_4@C-reinforced PbO_2-coated electrode (4 g L^{-1}) was reduced by

315.369 kW h compared with the Pb–0.6%Sb/α-PbO$_2$/β-PbO$_2$ coated electrode and by 455.501 kW h compared with the Pb–0.76%Ag alloy, indicating a prominent energy-saving effect in the zinc electrowinning process.

$$\eta = m/(qItn) \times 100\% \qquad (8)$$

$$W = 819.76v/\eta \qquad (9)$$

4. Conclusion

To sum up, a layered Co$_3$O$_4$@C-reinforced PbO$_2$-coated electrode was synthesized by a simple two-step pyrolysis-oxidation and following electrodeposition process on a Pb–0.6%Sb substrate. The prepared Co$_3$O$_4$@C-reinforced PbO$_2$-coated electrode showed a minimum overpotential of 517 mV at 500 A m^{-2} and a Tafel slope of 0.152 V dec^{-1} at an optimum Co$_3$O$_4$@C concentration of 4 g L^{-1}. It also exhibited a low R_{ct} value of 2.18 Ω and a satisfactory C_{dl} value of 24.36 mF cm^{-2}, resulting in a boost in OER activity. In the zinc electrowinning simulation experiment, the Co$_3$O$_4$@C-reinforced PbO$_2$-coated electrode (4 g L^{-1}) showed the most excellent stability and various zinc electrowinning parameters compared to the other two unreinforced electrodes. Moreover, the Co$_3$O$_4$@C-reinforced PbO$_2$-coated electrode (4 g L^{-1}) possessed a service life of up to 93 hours under high current density and high acidity of 20 000 A m^{-2} and 1.53 M H$_2$SO$_4$.

Author contributions

Wenhao Jiang: data processing and analysis, experimental operation, manuscript writing and revising. Junli Wang, Xuanbing Wang: materials characterization, data analysis, manuscript reviewing. Xuanbing Wuan, Jiang Liao: data analysis, discussing the research idea, manuscript reviewing. Jinlong Wei: data analysis, manuscript reviewing. Ruidong Xu, Linjing Yang: discussing the research idea, manuscript reviewing and editing.

Conflicts of interest

There are no conflicts to declare.

Acknowledgements

References

1 L. Jin, H. Huang, Y. Fei, H.-t. Yang, H.-y. Zhang and Z.-c. Guo, *Hydrometallurgy*, 2018, **176**, 201–207.

2 H.-h. Li, T.-c. Yuan, R.-d. Li, W.-j. Wang, D. Zheng and J.-w. Yuan, *Trans. Nonferrous Met. Soc. China*, 2019, **29**, 2422–2429.

3 B. Shen, Y. He, W. Li, Z. Wang, L. Yu, Y. Jiang, X. Liu, J. Kang, H. Gao and N. Lin, *Mater. Des.*, 2020, **191**, 108645.

4 S. He, R. Xu, L. Sun, Y. Fan, Z. Zhao, H. Liu and H. Lv, *Hydrometallurgy*, 2020, **194**, 105357.

5 A. J. Bloomfield, S. W. Sheehan, S. L. Collom and P. T. Anastas, *ACS Sustainable Chem. Eng.*, 2015, **3**, 1234–1240.

6 G. Hu, R.-d. Xu, S.-w. He, B.-m. Chen, H.-t. Yang, B.-h. Yu and Q. Liu, *Trans. Nonferrous Met. Soc. China*, 2015, **25**, 2095–2102.

7 H. You, Z. Chen, Q. Yu, W. Zhu, B. Chen, Z. Lv, Q. Hu, Y. Liu, Z. Zheng, S. Li and F. Yeasmin, *Sep. Purif. Technol.*, 2021, **276**, 119406.

8 Z. M. Alimirzaeva, A. B. Isaev, N. S. Shabanov, A. G. Magomedova, M. V. Kadiev and K. Kaviyarasu, *Mater. Today: Proc.*, 2021, **36**, 325–327.

9 A. M. Ali, S. A. M. Issa, M. R. Ahmed, Y. B. Saddeek, M. H. M. Zaid, M. Sayed, H. H. Somaily, H. O. Tekin, H. A. A. Sidek, K. A. Matori and H. M. H. Zakaly, *J. Mater. Res. Technol.*, 2020, **9**, 13956–13962.

10 A. Ansari and D. Nematollahi, *Water Res.*, 2018, **144**, 462–473.

11 X. Qian, K. Peng, L. Xu, S. Tang, W. Wang, M. Zhang and J. Niu, *Chem. Eng. J.*, 2022, **429**, 132309.

12 Y. Wang, M. Chen, C. Wang, X. Meng, W. Zhang, Z. Chen and J. Crittenden, *Chem. Eng. J.*, 2019, **374**, 626–636.

13 Y. Qiu, J. A. Lopez-Ruiz, U. Sanyal, E. Andrews, O. Y. Gutiérrez and J. D. Holladay, *Appl. Catal., B*, 2020, **277**, 119277.

14 W. J. de Santana Mota, G. de Oliveira Santiago Santos, A. Resende Dória, M. Rubens dos Reis Souza, L. C. Krause, G. R. Salazar-Banda, K. I. Barrios Eguiluz, J. A. López and M. L. Hernández-Macedo, *Chemosphere*, 2021, **279**, 130875.

15 C. Chen, R. Xu, X. Wang, W. Jiang, S. Feng and A. Ju, *Ceram. Int.*, 2021, **47**, 25350–25362.

16 Z. Xiangyang, W. Shuai, M. Chiyuan, L. Bo, W. Hui, Y. Juan, G. Zhongcheng and C. Buming, *Rare Met. Mater. Eng.*, 2018, **47**, 1999–2004.

17 B. Monahov, D. Pavlov and D. Petrov, *J. Power Sources*, 2000, **85**, 59–62.

18 C. Liao, B. Yang, N. Zhang, M. Liu, G. Chen, X. Jiang, G. Chen, J. Yang, X. Liu, T.-S. Chan, Y.-J. Lu, R. Ma and W. Zhou, *Adv. Funct. Mater.*, 2019, **29**, 1904020.

19 C. Liao, Z. Xiao, N. Zhang, B. Liang, G. Chen, W. Wu, J. Pan, M. Liu, X.-R. Zheng, Q. Kang, X. Cao, X. Liu and R. Ma, *Chem. Commun.*, 2021, **57**, 9060–9063.

20 O. Shmychkova, T. Luk'yanenko, R. Amadelli and A. Velichenko, *J. Electroanal. Chem.*, 2014, **717–718**, 196–201.

21 O. Kosohin, O. Makohoniuk and A. Kushmyruk, *Mater. Today: Proc.*, 2019, **6**, 219–226.

22 H. Mo, Y. Tang, N. Wang, M. Zhang, H. Cheng, Y. Chen, P. Wan, Y. Sun, S. Liu and L. Wang, *J. Solid State Electrochem.*, 2016, **20**, 2179–2189.

23 C.-b. Tang, Y.-x. Lu, F. Wang, H. Niu, L.-h. Yu and J.-q. Xue, *Electrochim. Acta*, 2020, **331**, 135381.

24 H.-t. Yang, B.-m. Chen, Z.-c. Guo, H.-r. Liu, Y.-c. Zhang, H. Huang, R.-d. Xu and R.-c. Fu, *Trans. Nonferrous Met. Soc. China*, 2014, **24**, 3394–3404.

25 X. Duan, F. Ma, Z. Yuan, L. Chang and X. Jin, *J. Electroanal. Chem.*, 2012, **677–680**, 90–100.

26 B. Yang, N. Zhang, G. Chen, K. Liu, J. Yang, A. Pan, M. Liu, X. Liu, R. Ma and T. Qiu, *Appl. Catal., B*, 2020, **260**, 118184.

27 Y. Wang, B. Yu, K. Liu, X. Yang, M. Liu, T.-S. Chan, X. Qiu, J. Li and W. Li, *J. Mater. Chem. A*, 2020, **8**, 2131–2139.

28 G. Zhang, J. Yang, H. Wang, H. Chen, J. Yang and F. Pan, *ACS Appl. Mater. Interfaces*, 2017, **9**, 16159–16167.

29 Z. Wang, W. Xu, X. Chen, Y. Peng, Y. Song, C. Lv, H. Liu, J. Sun, D. Yuan, X. Li, X. Guo, D. Yang and L. Zhang, *Adv. Funct. Mater.*, 2019, **29**, 1902875.

30 M. Zhang, J. Shi, Y. Sun, W. Ning and Z. Hou, *Catal. Commun.*, 2015, **70**, 72–76.

31 B. Sun, S. Lou, W. Zheng, Z. Qian, C. Cui, P. Zuo, C. Du, J. Xie, J. Wang and G. Yin, *Nano Energy*, 2020, **78**, 105366.

32 C. Zhang, J. Liu, Y. Ye, Z. Aslam, R. Brydson and C. Liang, *ACS Appl. Mater. Interfaces*, 2018, **10**, 2423–2429.

33 Y. Yao, T. Zhou, C. Zhao, Q. Jing and Y. Wang, *Electrochim. Acta*, 2013, **99**, 225–229.

34 A. B. Velichenko, R. Amadelli, E. V. Gruzdeva, T. V. Luk'yanenko and F. I. Danilov, *J. Power Sources*, 2009, **191**, 103–110.

35 R. Barik, A. Raulo, S. Jha, B. Nandan and P. P. Ingole, *ACS Appl. Energy Mater.*, 2020, **3**, 11002–11014.

36 L. Yang, W. Zhou, J. Lu, D. Hou, Y. Ke, G. Li, Z. Tang, X. Kang and S. Chen, *Nano Energy*, 2016, **22**, 490–498.

37 A. Al Nafiey, A. Addad, B. Sieber, G. Chastanet, A. Barras, S. Szunerits and R. Boukherroub, *Chem. Eng. J.*, 2017, **322**, 375–384.

38 L. Ma, H. Zhou, X. Shen, Q. Chen, G. Zhu and Z. Ji, *RSC Adv.*, 2014, **4**, 53180–53187.

39 D. He, X. Song, W. Li, C. Tang, J. Liu, Z. Ke, C. Jiang and X. Xiao, *Angew. Chem., Int. Ed.*, 2020, **59**, 6929–6935.

40 X. Li, S. You, J. Du, Y. Dai, H. Chen, Z. Cai, N. Ren and J. Zou, *J. Mater. Chem. A*, 2019, **7**, 25853–25864.

41 K. Kumar, C. Canaff, J. Rousseau, S. Arrii-Clacens, T. W. Napporn, A. Habrioux and K. B. Kokoh, *J. Phys. Chem. C*, 2016, **120**, 7949–7958.

42 R. Li, Y. Huang, D. Zhu, W. Ho, J. Cao and S. Lee, *Environ. Sci. Technol.*, 2021, **55**, 4054–4063.

43 J. Xiao, C. Chen, J. Xi, Y. Xu, F. Xiao, S. Wang and S. Yang, *Nanoscale*, 2015, **7**, 7056–7064.

44 G. Darabizad, M. S. Rahmanifar, M. F. Mousavi and A. Pendashteh, *Mater. Chem. Phys.*, 2015, **156**, 121–128.

45 U. Holzwarth and N. Gibson, *Nat. Nanotechnol.*, 2011, **6**, 534.

46 X. Duan, F. Xu, Y. Wang, Y. Chen and L. Chang, *Electrochim. Acta*, 2018, **282**, 662–671.

47 H. Liu, A. M. Kuznetsov, A. N. Masliy, J. F. Ferguson and G. V. Korshin, *Environ. Sci. Technol.*, 2012, **46**, 1430–1438.

48 Y. Lai, Y. Li, L. Jiang, W. Xu, X. Lv, J. Li and Y. Liu, *J. Electroanal. Chem.*, 2012, **671**, 16–23.

49 J. Aromaa and O. Forsén, *Electrochim. Acta*, 2006, **51**, 6104–6110.

50 F. Shen and K. Lu, *ACS Appl. Mater. Interfaces*, 2017, **9**, 6022–6029.

51 B. Hirschorn, M. E. Orazem, B. Tribollet, V. Vivier, I. Frateur and M. Musiani, *Electrochim. Acta*, 2010, **55**, 6218–6227.

52 L. Xu, Y. Wang and W. Zhang, *RSC Adv.*, 2019, **9**, 39242–39251.

53 L. Xu, Y. Yi, G. Liang and W. Zhang, *Electroanalysis*, 2020, **32**, 1370–1378.

54 Z. Zhao, L. Liu, L. Min, W. Zhang and Y. Wang, *Materials*, 2021, **14**, 2841.